

Article

Significantly Enhanced Self-Cleaning Capability in Anatase TiO₂ for the Bleaching of Organic Dyes and Glazes

Tiangui Zhao, Tihao Cao, Qifu Bao *, Weixia Dong *, Ping Li, Xingyong Gu, Yunzi Liang and Jianer Zhou

School of Materials Science and Engineering, Jingdezhen Ceramic University, Jingdezhen 333403, China

* Correspondence: bqf2002@hotmail.com (Q.B.); dongweixia@jci.edu.cn (W.D.)

Abstract: In this study, the Mg²⁺-doped anatase TiO₂ phase was synthesized via the solvothermal method by changing the ratio of deionized water and absolute ethanol ($V_{\text{water}}/V_{\text{ethanol}}$). This enhances the bleaching efficiency under visible light. The crystal structure, morphology, and photocatalytic properties of Mg-doped TiO₂ were characterized by X-ray diffraction, scanning electron microscopy, high-resolution transmission electron microscopy, N₂ adsorption-desorption, UV-Vis spectroscopy analysis, etc. Results showed that the photocatalytic activity of the Mg²⁺-doped TiO₂ sample was effectively improved, and the morphology, specific surface area, and porosity of TiO₂ could be controlled by $V_{\text{water}}/V_{\text{ethanol}}$. Compared with the Mg-undoped TiO₂ sample, Mg-doped TiO₂ samples have higher photocatalytic properties due to pure anatase phase formation. The Mg-doped TiO₂ sample was synthesized at $V_{\text{water}}/V_{\text{ethanol}}$ of 12.5:2.5, which has the highest bleaching rate of 99.5% for the rhodamine B dye during 80 min under visible light. Adding Mg²⁺-doped TiO₂ into the phase-separated glaze is an essential factor for enhancing the self-cleaning capability. The glaze samples fired at 1180 °C achieved a water contact angle of 5.623° at room temperature and had high stain resistance (the blot floats as a whole after meeting the water).

Keywords: solvothermal method; Mg-doped TiO₂; $V_{\text{water}}/V_{\text{ethanol}}$; self-cleaning properties; visible light



Citation: Zhao, T.; Cao, T.; Bao, Q.; Dong, W.; Li, P.; Gu, X.; Liang, Y.; Zhou, J. Significantly Enhanced Self-Cleaning Capability in Anatase TiO₂ for the Bleaching of Organic Dyes and Glazes. *Inorganics* **2023**, *11*, 341. <https://doi.org/10.3390/inorganics11080341>

Academic Editors: Roberto Nisticò and Silvia Mostoni

Received: 25 June 2023

Revised: 15 August 2023

Accepted: 15 August 2023

Published: 18 August 2023



Copyright: © 2023 by the authors. Licensee MDPI, Basel, Switzerland. This article is an open access article distributed under the terms and conditions of the Creative Commons Attribution (CC BY) license (<https://creativecommons.org/licenses/by/4.0/>).

1. Introduction

With the deterioration of environmental pollution, low-consumption and high-efficiency pollution technologies have received more attention [1,2]. As the durative utilizes clean energy, solar energy has vast potential for exploitation and application. Titanium dioxide is an important photocatalyst that has been widely studied because of its high activity, non-toxic characteristics, environmental friendliness, and good chemical stability [3–6]. As the energy barrier of the metastable phase was less than that of the stability phase, it was more likely to excite electrons and holes for the metastable phase [7,8]. Hence, anatase TiO₂ is considered to be the best photocatalyst of all of the structures of TiO₂ [9,10]. It can fully effectively utilize UV light from sunlight [11–13]. Several factors affect anatase TiO₂ photoactivity, such as crystal size, specific surface area, and crystallinity [14–16]. The performance of the TiO₂ was optimized by doping [17–20], loading [21,22], and thin-film preparation [23,24]. Available studies indicated that some ions could enter the lattice as substitutional or interstitial; the titanium ions are substituted by metal ions in the crystal lattices. Some studies illustrate that rare-metal-ion-doped titania nanoparticles were prepared by the hydrothermal method, and their photocatalytic performance was greatly improved under UV irradiation [25,26]. At present, there exist a few studies concerning magnesium-ion-doped TiO₂ obtained by the sol-gel reaction synthesis route and the solvothermal method [27,28], but its processing is complex and needs HF as a capping agent to form the anatase phase. It would therefore be interesting to investigate how a simple method can be used for preparing a glaze containing Mg(II)-doped anatase that is stable in a medium-/high-temperature (>1000 °C) ceramic glaze [29] and has self-cleaning properties, as anatase TiO₂ has a nanometer size.

This study presents the simple synthetic procedure of producing Mg-doped TiO₂ anatase samples without surfactants or templates and evaluates the influence of the structure and $V_{\text{water}}/V_{\text{ethanol}}$ on their photocatalytic activity in decomposing rhodamine B (RhB). The self-cleaning activities of Mg-doped and undoped TiO₂ anatase glaze samples are evaluated by comparing their anti-pollution ability.

2. Experimental Section

2.1. Preparation of the Samples

The samples, with various deionized water and absolute ethanol contents, were prepared from tetrabutyl titanate (TBOT), MgCl₂•6H₂O, and NaOH using the hydrothermal method. In a typical synthesis, firstly, solution A was made, which included MgCl₂•6H₂O, deionized water, and absolute ethanol. Subsequently, solution B was made, which included TBOT and ethanol. Finally, suspension C was prepared by dripping solution B into system A. The molar ratio of MgCl₂•6H₂O:TBOT:ethanol: water was 0.03:1:10:50. After 15 min, after adding suspension C into the reactor, it was heated at 180 °C for 36 h and then naturally cooled to room temperature. The final sample obtained was centrifuged and washed with deionized water and absolute ethanol. The photocatalytic properties of the samples were investigated by changing the molar ratio of water/ethanol ($V_{\text{water}}:V_{\text{ethanol}}$), keeping other experimental parameters unchanged. Figure 1 is the schematic diagram of Mg-doped TiO₂ sample preparation.

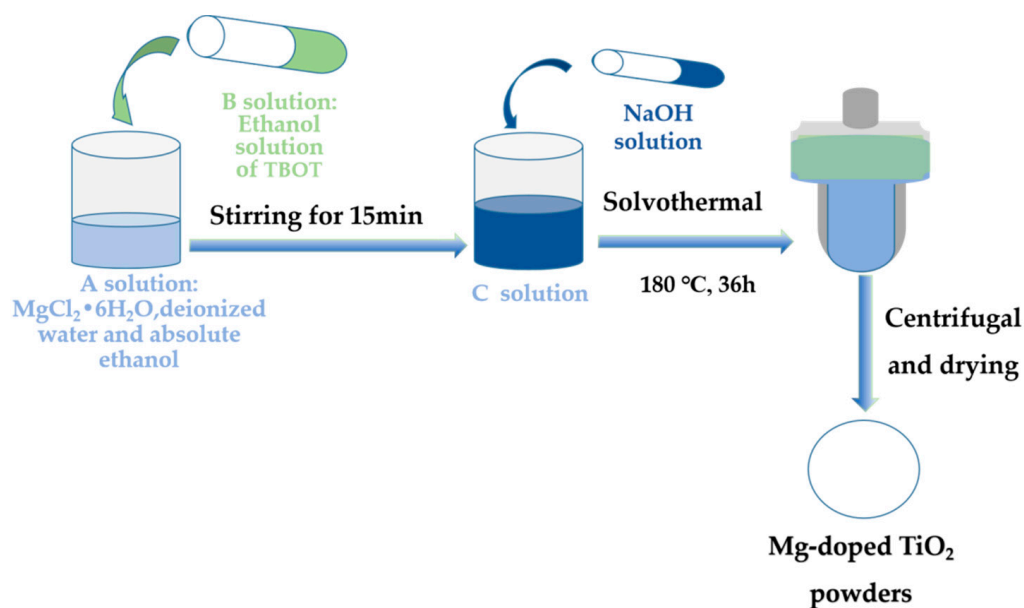


Figure 1. Schematic diagram of Mg-doped TiO₂ sample preparation.

The Mg-doped TiO₂ in the glaze sample was fabricated by sintering at 1180~1200 °C using raw powders, i.e., 95% of the as-prepared Kaolin clay was subjected to phase separation melting at 1500 °C for 4 h and 5% by adding 5% Mg-doped TiO₂ ($V_{\text{water}}/V_{\text{ethanol}}$ of 12.5:2.5) photocatalysts, and the self-cleaning and hyper-hydrophilic properties of the fired glaze samples were characterized and tested, respectively. Figure 2 is the schematic diagram of the glaze firing processes.

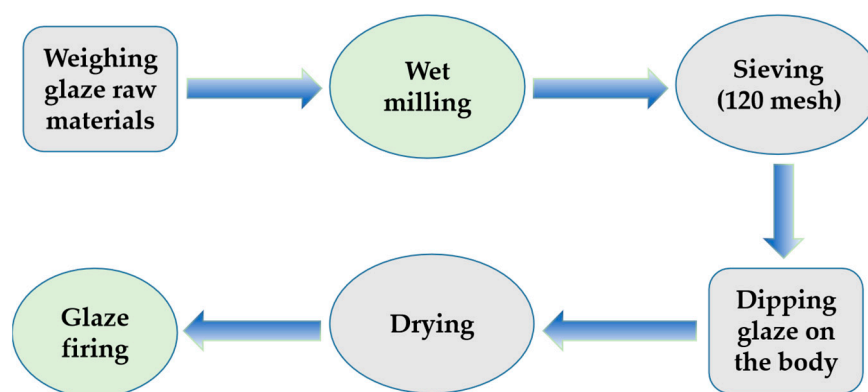


Figure 2. Schematic diagram of the glaze firing processes.

2.2. Characterization of the Samples

The crystalline phase was identified by X-ray diffractometer (XRD, D8 Advance Bruker AXS, Germany) using Cu K α radiation. Compared with the standard pattern in the XRD standard database, including JCPDS (i.e., PDF cards), the phase composition of the sample was analyzed using Jade 6.0 software. Photocatalyst morphology was investigated by scanning electron microscopy (SEM, JSM-6700F, Japan) using a device equipped with an EDS system operating at an accelerating voltage of 5.0 kV or 15 kV (15 kV for EDS). The crystal surface of nanocrystals was evaluated by high-resolution microscopy. The microstructures of the samples were studied by transmission electron microscopy (TEM, FEI Tecnai G2 F-30, Holland) and high-resolution transmission electron microscopy (HRTEM, FEI Tecnai G2 F-30, Holland) at accelerating voltages of 160 kV and 200 kV, respectively. The valence states of the samples were characterized by X-ray photoelectron spectroscopy (XPS, ESCALAB Xi+, United States) using Al K α radiation. The specific surface areas were determined by the Brunauer–Emmett–Teller method, and the pore size was determined by the Barrett–Joyner–Hallenda method. Nitrogen adsorption-desorption isotherms were collected on a Micromeritics TriStar ii 3020 analyzer at 77 K. The analysis of samples by UV-Vis diffuse reflectance spectroscopy was carried out. The hydrophilicity of the samples was tested by a contact angle meter (JGW-360D, China).

2.3. Photocatalytic Activity of the Samples

The photocatalytic activity of the TiO₂ was evaluated by bleaching the RhB with a concentration of 10^{−4} mol/L. The total volume of RhB was 50 mL, irradiated with 0.05 g of the photocatalyst and a 500 W Xeon light with a cut-off filter of 420 nm. This was to prove that the RhB was exhibiting bleaching rather than adsorption after the dark experiment was carried out. Samples were taken out at 20 min intervals and analyzed with a spectrophotometer. The photocatalytic activity was characterized by the apparent first-order rate constant k , as in equation $k = \ln(A_0/A)$, where A was the absorbance of RhB at 553 nm after bleaching and A_0 was the absorbance of the initial RhB solution at 553 nm.

3. Results and Discussion

3.1. Structural and Morphology

The crystal phase of the samples was studied as shown in Figure 3. The obtained diffraction peak of the doped TiO₂ matched very well with the standard values (PDF-#21-1272) and the diffraction peaks at $2\theta = 25.281(101)$, $37.800(004)$, $48.049(200)$, $53.890(105)$, and $62.688(204)$, illustrating that the samples were in the anatase phase. However, the obtained undoped TiO₂ was in a mixed phase of anatase and brookite. The cell volume was calculated by Fourier synthesis with the program SHELXS-97 [30]. When the solvent was water, the sample consisted of nanoparticles 10~20 nm in mean size, as determined by Nano Measurer 1.2 software using 10 nanoparticles. The average crystallite size of TiO₂ samples with different Mg-doped ions was calculated by XRD–Scherrer formula:

$d = 0.91 \lambda / \beta \cos \theta$, where d is the mean crystallite size, k is 0.9, λ is the wavelength of Cu K α (i.e., $\lambda = 0.15420$ nm), β is the full width at half maximum intensity of the peak (FWHM) in radian, and θ is Bragg's diffraction angle [31]. The crystallite size and cell volume were calculated as shown Table 1. When increasing $V_{\text{water}}/V_{\text{ethanol}}$, there are differences in the diffraction peak intensity and minor shifts in the peak occur, which indicates a reduction in crystalline size and an increase in the volume of unit cells (Table 1). Since the ionic radius of Mg^{2+} (0.072 nm) is close to that of Ti^{4+} (0.061 nm), Mg^{2+} easily enters the TiO_2 lattice [32] and the lattice volume increases (Table 1), indicating that the formation of a crystal defect. Based on the experimental results, the formation of the crystal defect promotes the formation of the anatase phase, which is accordance with the reported literature [27,29]. Hence, after the addition of the magnesium source, a pure-anatase TiO_2 phase appears. The intensity of the (004) direction is significantly enhanced compared to undoped TiO_2 . In addition, the FWHM of the (101) peak was calculated by using Lorentz fitting. According to the Scherrer formula, $d = 0.91 \lambda / \beta \cos \theta$, the crystallite size was calculated; it is shown in Table 1.

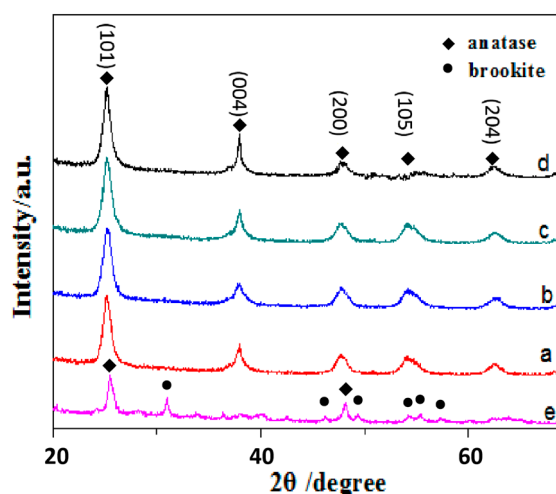


Figure 3. XRD patterns of the samples with different volume ratios of water: ethanol: (a) 15: 0, (b) 12.5:2.5, (c) 10:5, (d) 7.5:7.5, (e) undoped TiO_2 (12.5:2.5).

Table 1. Effect of different ratios of water: ethanol in the solvent on the crystal size, BET surface area, pore size, pore volume, and cell volume of Mg-doped TiO_2 .

| | $V_{\text{water}}/V_{\text{ethanol}}$ | Crystal Size (nm) | BET (m^2/g) | Pore Size (nm) | Pore Volume (cm^3/g) | Cell Volume \AA^3 |
|-------------------------|---------------------------------------|-------------------|-------------------------------|----------------|--|----------------------------|
| Mg-doped TiO_2 | 15:0 | 13.6 | 152 | 13.8 | 0.415 | 136.458 |
| | 12.5:2.5 | 13.2 | 148 | 12.5 | 0.402 | 136.315 |
| | 10:5 | 10.3 | 105 | 12.4 | 0.378 | 136.452 |
| | 7.5:7.5 | 8.1 | 101 | 12.0 | 0.350 | 136.689 |
| Pure TiO_2 | 12.5:2.5 | 14.0 | 98 | 11.2 | 0.340 | 136.089 |

Figure 4 shows SEM images of the as-synthesized samples. When the solvent was water, the sample consisted of nanoparticles 5–10 nm in size. When the $V_{\text{water}}/V_{\text{ethanol}}$ ratio was 12.5:2.5, agglomerated nanoparticles had a grape-like morphology (Figure 4b). With the increase in ethanol dosage, nanoparticles increased (Figure 4c,d). The experimental results show that the morphology of the samples was greatly affected by $V_{\text{water}}/V_{\text{ethanol}}$. Their morphology is determined by the relationship between crystal formation and growth. Moreover, crystal growth is influenced by the adsorption of certain crystalline facets into OH^- . This adsorption hinders the growth of these facets, resulting in different rates of crystalline growth. Ethanol is a typical polar solvent and amphiphilic molecule. It

was vertically adsorbed on the hydrophilic surface of the TiO₂ particles, forming a two-amphiphilic bilayer, which limited the immersion of the water molecule in the hydrophilic side surface and the TiO₂ particles [33]. The rapid hydrolysis of TBOT promoted the rapid generation of TiO₂, which led to TiO₂ particle agglomeration with an increase in $V_{\text{water}}/V_{\text{ethanol}}$. Figure 5a,b show TEM and the corresponding SAED pattern (inset) and HRTEM images of the sample prepared at $V_{\text{water}}/V_{\text{ethanol}} = 12.5:2.5$. From Figure 5a, it is observed that the aggregated particles in Figure 4b consist of nanoparticles. The major diffraction rings for the crystal surface at (101), (004), and (105) match well with XRD analysis. The d spacing is 0.325 nm (Figure 5b), and it matches well with the lattice spacing of anatase TiO₂ (101). Furthermore, the corresponding EDX spectrum shown in Figures 5c and S1 verifies the existence of Mg, Ti, and O ions. Other impurities were not detected in the EDX spectra.

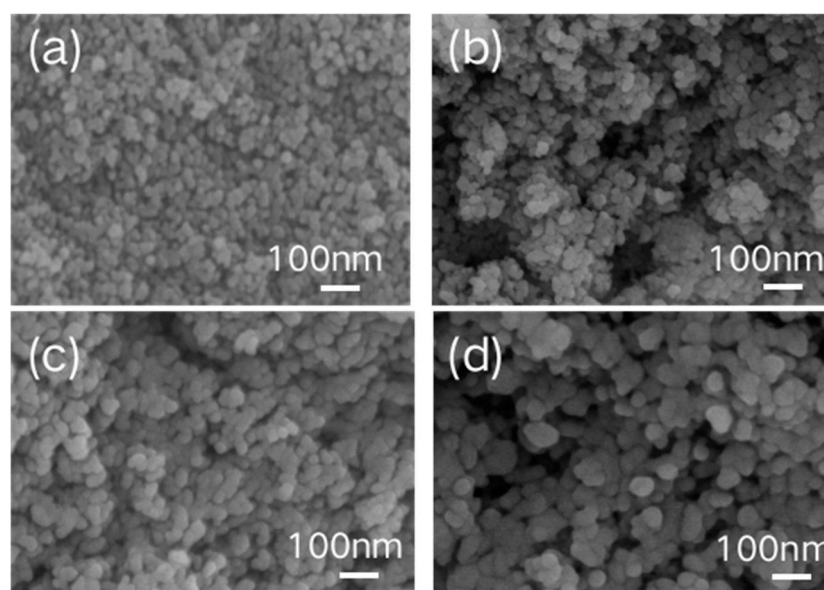


Figure 4. SEM images of TiO₂ with different volume ratios of water: ethanol (a) 15:0, (b) 12.5:2.5, (c) 10:5, (d) 7.5:7.5.

As can be seen from Table 1 and Figure 3, the morphologies of the samples strongly depend on Mg-doped ions and $V_{\text{water}}/V_{\text{ethanol}}$. Because the current system contains ethanol, water, Mg-doped ions, and TBOT, we can reasonably assume that the formation of anatase TiO₂ is due to the dehydrating condensation between $\text{Ti}(\text{OH})_6^{2-}$ and Mg-doped ions under solvothermal conditions [34]. Thus, due to the formation of a lower number of active OH^- ions and a lower number of soluble species, $\text{Ti}(\text{OH})_6^{2-}$ and TiO_6 octahedrons in one cluster may construct a chain via the corner-sharing of $\text{Ti}(\text{OH})_6^{2-}$ growth units. Due to doped Mg ions entering the TiO₂ lattice, resulting in TiO_6 octahedron lattice distortion (Table 1) and an increase in the charge density of Ti and reduction in the electron density of oxygen, the preferred TiO_6 octahedron chain-shaped clusters further adsorb OH^- soluble species into the (101) plane (Figure 5b) and anatase TiO₂ monomers form through a dehydrating condensation process. Therefore, these planes could be freely bonded by interactions between OH^- and nuclei to obtain aggregated nanoparticles (Figure 4). The solubility of salt increases with the dielectric constant of the solvent [35], and the dielectric constant of water is bigger than that of ethanol. When $V_{\text{water}}/V_{\text{ethanol}}$ decreases, that is, ethanol content increases, this could decrease the solubility of the precursor and increase the viscosity of the solution, thereby decreasing the diffusion ability of $\text{Ti}(\text{OH})_6^{2-}$ ions and causing the crystal size of the TiO₂ sample to decrease (Table 1).

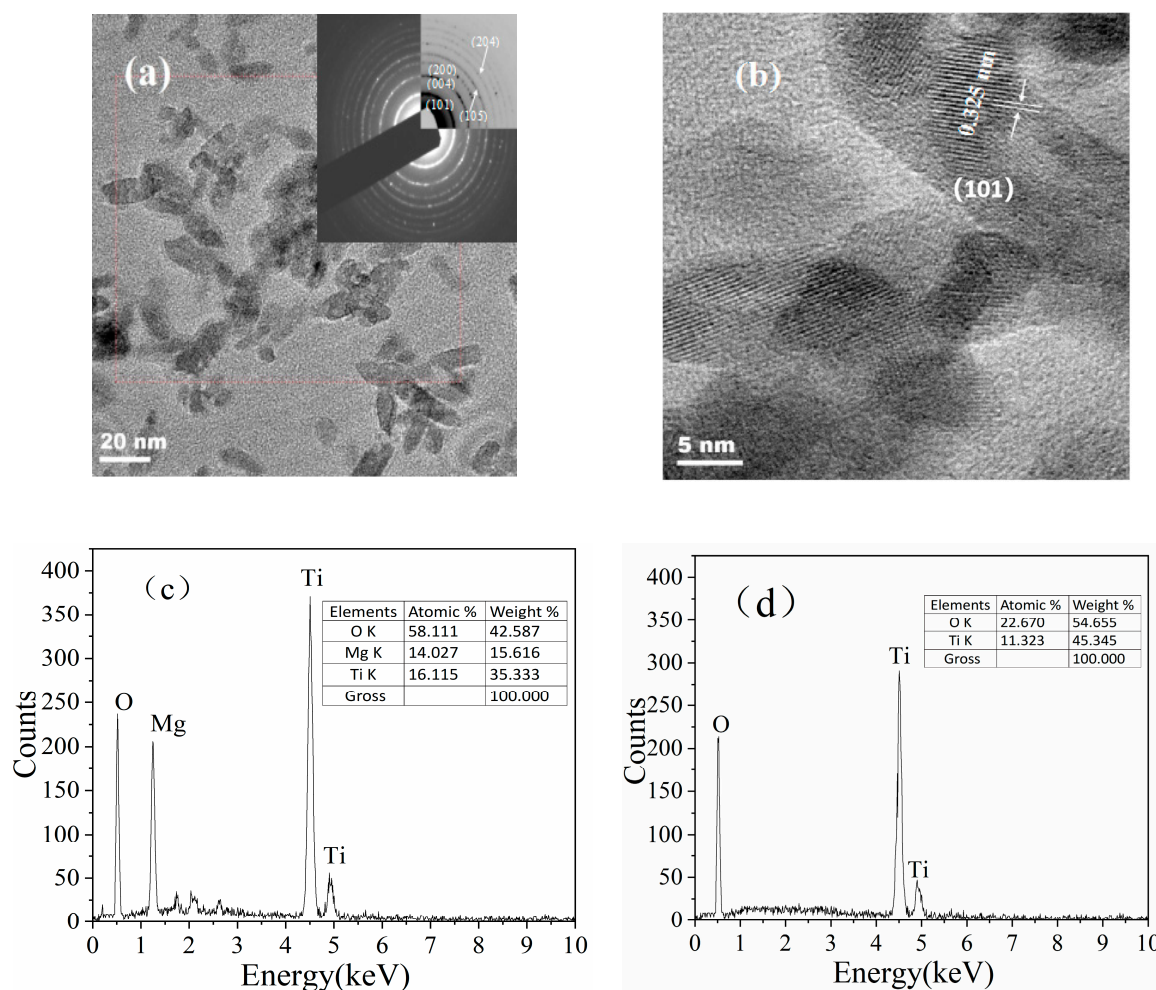


Figure 5. (a) TEM images and SAED pattern, (b) HRTEM images, (c,d) EDX spectra. (a–c) Mg-doped sample prepared using $V_{\text{water}}/V_{\text{ethanol}} = 12.5:2.5$, (d) pure TiO₂ sample prepared using $V_{\text{water}}/V_{\text{ethanol}} = 12.5:2.5$.

Figure 6 shows XPS spectra of pure and Mg-doped TiO₂ samples. Peaks located around 457 eV and 464 eV resulted from Ti 2p_{3/2} and Ti 2p_{1/2}, respectively, corresponding to the oxidation state of Ti⁴⁺. Meanwhile, due to the partial substitution of Ti⁴⁺ ions by Mg²⁺, the binding energy of Ti decreases, thus increasing the charge density of Ti. The binding energy of O 1s in the pure TiO₂ sample is 529.8 eV, owing to the intrinsic binding energy of oxygen in TiO₂. The Mg-doped TiO₂ sample shows a shoulder peak near 532.3 eV in addition to the intrinsic binding energy of O 1s (shown in Figure 6b). This may be due to the addition of small amounts of Mg atoms, causing new oxygen vacancies [36]. Oxygen vacancies in TiO₂ are usually created in doped TiO₂ to maintain charge neutrality and improve the service life of the photocatalyst [37]. When oxygen vacancies are generated, a higher energy peak can be seen due to the decrease in the electron density of oxygen [37]. A peak at 49.93 eV was associated with Mg 2p, which is further verified by the incorporation of Mg²⁺ into the titanium dioxide lattice.

Figure 7 shows the typical FT-IR spectrum of undoped TiO₂ and Mg-doped TiO₂ samples with different $V_{\text{water}}/V_{\text{ethanol}}$ ratios. All samples have absorption peaks at 3380 cm⁻¹ and 1640 cm⁻¹, corresponding to O-H stretching vibration and bending vibration, respectively [38]. For the undoped TiO₂ sample, the bands at 1450 cm⁻¹ and 1538 cm⁻¹ are attributed to the H-O-H bending of the lattice water [39]. The band centered at 510 cm⁻¹ is due to isolated tetrahedral TiO₄ stretching vibrations and only occurs in the pure TiO₂ sample [40]. As a result of Mg-doping, the bands at 1065 cm⁻¹ and 458 cm⁻¹ show the

vibration of Ti-O-Mg [41]. With the increase in ethanol content, the intensities of the absorption peaks at 3380 cm^{-1} and 458 cm^{-1} increase, respectively. This indicates that Mg ions are doped into the lattice of TiO_2 , and the HRTEM, TEM, and XRD results further confirmed this point.

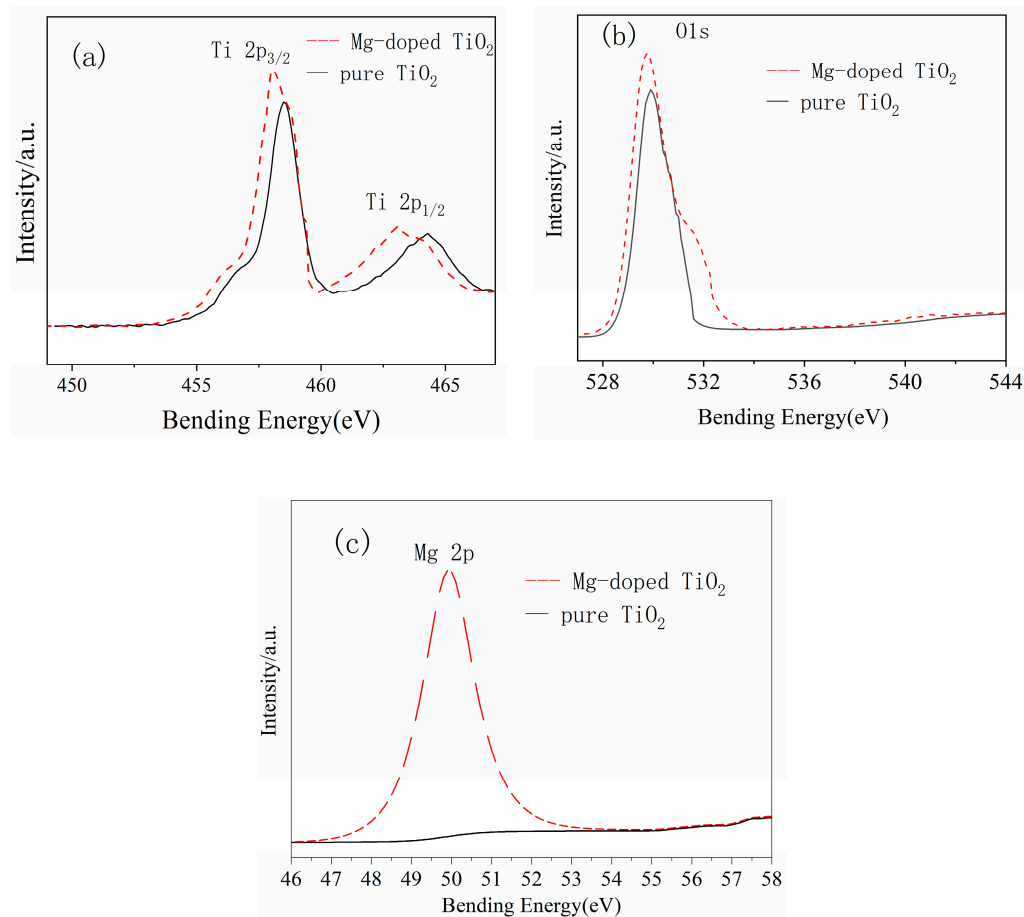


Figure 6. XPS spectra of the undoped TiO_2 and Mg-doped TiO_2 samples prepared using $V_{\text{water}}/V_{\text{ethanol}}$ ratio of 15:0 (a) Ti, (b) O, (c) Mg.

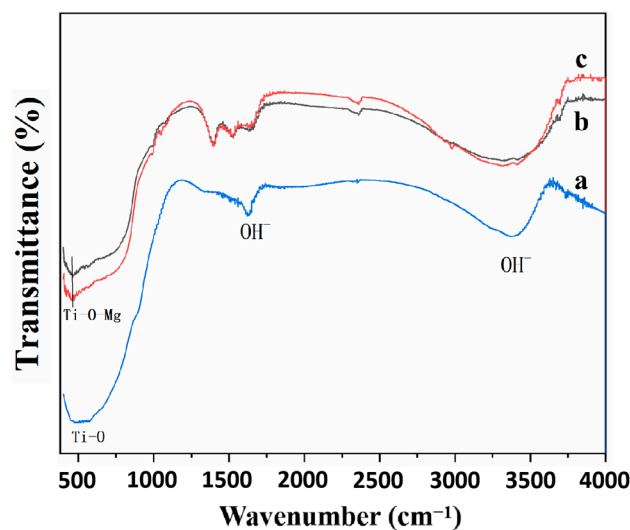


Figure 7. FT-IR spectrum of the typical samples: (a) undoped TiO_2 , (b) Mg-doped TiO_2 samples prepared using $V_{\text{water}}/V_{\text{ethanol}}$ ratio of 15:0, (c) Mg-doped TiO_2 samples prepared using $V_{\text{water}}/V_{\text{ethanol}}$ ratio of 12.5:2.5.

3.2. BET Analysis

Figure 8 shows the BET analysis of the samples using nitrogen adsorption-desorption. For all samples, the isotherms are type IV, and clear hysteresis loops can be identified. With the increase in $V_{\text{water}}/V_{\text{ethanol}}$, the BET surface area of the Mg-doped TiO_2 samples decreases. However, the pore volume and porosity of the samples exhibit a prominent enhancement compared with the undoped TiO_2 sample, as shown in Table 1 and Figure 8. The BJH average pore diameters, calculated from the adsorption branch of the isotherms, are 11.205 nm, 12.560 nm, 12.365 nm, and 12.807 nm for pure TiO_2 and Mg-doped TiO_2 samples prepared with different $V_{\text{water}}/V_{\text{ethanol}}$ ratios of 12.5:2.5, 10:5, and 7.5:7.5, respectively. The mesoporous structure is mainly due to the porous accumulation of nanoparticles [42]. The porosity increase is due to the crystal size reducing with the decrease in $V_{\text{water}}/V_{\text{ethanol}}$.

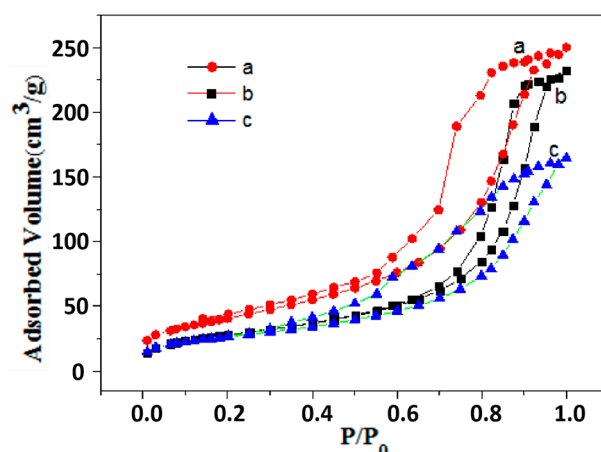


Figure 8. N_2 adsorption-desorption isotherm samples with different ratio of water: ethanol (a) doped TiO_2 12.5:2.5, (b) doped TiO_2 10:5, (c) undoped TiO_2 12.5:2.5.

3.3. Optical Properties

Figure 9 shows the UV-Visible diffuse reflectance spectra of TiO_2 . The absorption edge of doped TiO_2 had more of a blue shift than the undoped TiO_2 . The Kubelka–Munk formula, ($E(\text{eV}) = hc/\lambda$, $h = 6.626 \times 10^{-34} \text{ Js}$, $C = 3.0 \times 10^8 \text{ ms}^{-1}$), was used to acquire the exact band gap of TiO_2 from 3.26 eV to 3.13 eV, which can be attributed to the Mg^{2+} -doped TiO_2 in the framework. Since Mg^{2+} ions generated from oxygen vacancies are known to cause the photoexcitation of long-wavelength light, the UV-Vis absorption spectrum was inferred to verify the presence of Mg^{2+} in the TiO_2 -doped sample.

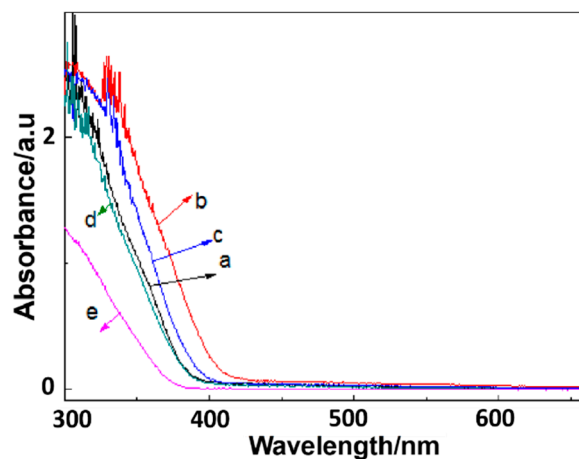


Figure 9. UV-Vis spectra of TiO_2 with different rate of water: ethanol (a) 15:0, (b) 12.5:2.5, (c) 10:5, (d) 7.5:7.5, (e) undoped TiO_2 12.5:2.5.

Moreover, from the spectrum, the energy gap of the semiconductor nanoparticles is related to the particle size. The band gap increases as the particle size decreases, resulting in a phenomenon known as a “blue shift” in light absorption at a specific wavelength due to the quantum size effect [43]. With the increase in ethanol content, the absorption edge of the doped TiO₂ is blue-shifted, illustrating the particle size reduction. The results obtained are well-matched with the sizes of the crystals that were measured. The band gap energies of the prepared TiO₂ doped by adding 0 to 7.5 mL ethanol were found to be 3.17 eV, 3.03 eV, 3.13 eV, and 3.25 eV, respectively. From Figure 4, it is clear that the size of anatase nanoparticles increases with the increase in ethanol content. Optical absorption is highly dependent on the internal structure of the material [44]. Compared with pure TiO₂, the longer-wavelength region of Mg-doped TiO₂ samples implies that the only possible transition is from the oxygen vacancies causing a red shift of the absorption edge (Figure 6), which also implies that Mg²⁺ has been incorporated into the lattice of TiO₂ (Table 1). From Figure 6, it can be observed that compared with the pure TiO₂ sample, the Ti and O binding energy in Mg-doped TiO₂ samples has been shifted to a lower energy and a higher energy peak, because some Ti⁴⁺ ions are replaced by Mg²⁺ ions in order to increase the charge density of Ti and reduce the electron density of oxygen [45]. The new oxygen vacancies are created through the doping of small amounts of Mg atoms [46]. For the Mg-doped TiO₂ sample, the peak of 49.9 eV is ascribed to Mg 2p (Figure 6c), which is consistent with the value of Mg²⁺ [27,41]. These observations further verify the existence of Mg²⁺ in the Mg-doped TiO₂ sample, which is consistent with XRD (Figure 3), increased cell volume (Table 1), and FT-IR spectrum (Figure 7).

3.4. Photocatalytic Activity

Figure 10 shows the photocatalytic bleaching of RhB through the as-prepared sample under visible light. As shown in Figure 10, RhB concentration is unchanged, illustrating that RhB adsorbed on the TiO₂ surface had reached equilibrium in 30 min. Figure 10b shows kinetic curves of $\ln(C_0/C)$ versus irradiation time during RhB bleaching under visible light irradiation. It has been found that the apparent rate constants [47] for the reaction of RhB with Mg-doped TiO₂ samples ($V_{\text{water}}/V_{\text{ethanol}} = 15:0, 12.5:2.5, 10:5, 7.5:7.5$) and Mg-undoped TiO₂ ($V_{\text{water}}/V_{\text{ethanol}} = 12.5:2.5$) were 0.01704, 0.06335, 0.04153, 0.01668, and 0.00203 min⁻¹, respectively, which illustrates that the photocatalytic activity of the samples was effectively improved by Mg²⁺-doping (due to pure anatase phase formation (Figure 3)). Moreover, the photocatalytic properties of Mg-doped TiO₂ can be further improved by changing the ratio of water to ethanol. The photocatalytic properties of the samples increased first and then decreased gradually with the increase in $V_{\text{water}}/V_{\text{ethanol}}$. When the $V_{\text{water}}/V_{\text{ethanol}}$ ratio was 12.5:2.5, Mg-doped TiO₂ had the maximum photocatalytic activity. In addition, by combining Table 1 with Figures 4 and 9, we can observe that the aggregated nanoparticles increase in size and thus E_g increases, which leads to the easy recombination of the electron and hole in the migration process, and therefore, the photocatalytic activity of the samples decreases with the increase in ethanol volume (i.e., $V_{\text{water}}/V_{\text{ethanol}}$ decreases). Although TiO₂ ($V_{\text{water}}/V_{\text{ethanol}} = 15:0$) has a larger specific surface area and smaller crystal size (Table 1) compared with the Mg-doped samples, the sample had lower porosity and pore size, which caused the decrease in the sample of RhB adsorption. This clearly indicates that the adsorption of samples was determined by the surface area and characteristics of the pore. Obviously, Mg-doped TiO₂ samples exhibited better photocatalytic activities than pure TiO₂ samples. The narrowing of the band gap is a result of Mg doping into the TiO₂ lattice, which enables the trapping of the photo-induced electron and facilitates the separation of electron-hole pairs (Figure 11a).

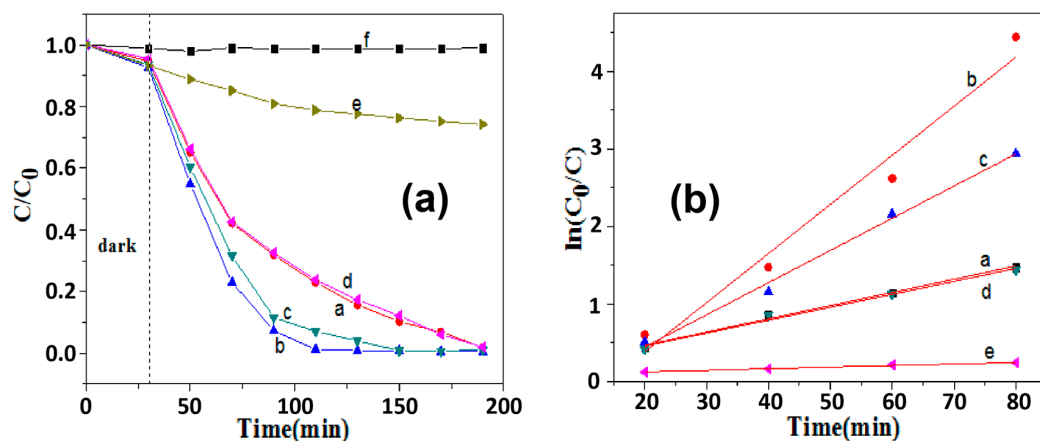


Figure 10. (a) Photocatalytic performance, (b) Kinetic curves of $\ln(C_0/C)$ as a function of irradiation time for RhB bleaching under visible light irradiation: (a) 15:0, (b) 12.5:2.5, (c) 10:5, (d) 7.5:7.5 of the Mg-doped samples, (e) Mg-undoped TiO_2 sample, (f) without photocatalyst.

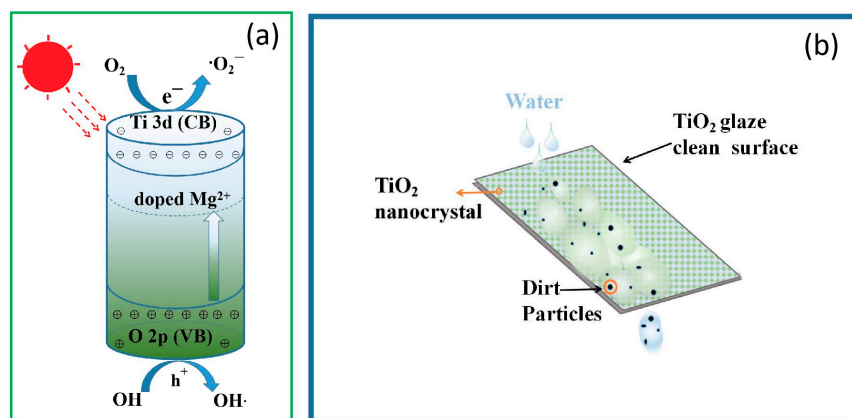


Figure 11. Schematic representation of photo processes using Mg-doped TiO_2 photocatalysts (a) and the self-cleaning process using Mg-doped TiO_2 in glaze sample (b), respectively.

3.5. Self-Cleaning Properties of Mg-Doped TiO_2 in Glaze Sample

It can be seen the wet angle of pure TiO_2 glaze samples is obviously higher than those of Mg-doped TiO_2 glaze samples (Figure 12). The super-hydrophilicity of Mg-doped TiO_2 glaze samples is attributed to several comprehensive factors. Based on the experimental results, Mg ions are helpful for the growth of the TiO_2 crystal grain, and thus separates the phase size in Mg-doped TiO_2 glaze more than pure TiO_2 . This makes the Mg-doped TiO_2 glaze surface rougher than that of the pure TiO_2 glaze (Figure 12). A large surface roughness could improve the hydrophilicity, according to the Wenzel equation (1): $\cos \theta_r = r \cos \theta$, where r denotes the surface roughness of the glaze, $\cos \theta$ is the classical contact angle depicted by the Young equation, and θ_r is the measured real contact angle. Moreover, the partial substitution of Mg^{2+} ions for Ti sites increases the slight TiO_2 lattice distortion, which is available for a low initial contact angle and hydrophilicity [48]. From Figure 12, it can be seen that the contact angles of Mg-doped TiO_2 samples are smaller than that of the pure TiO_2 glaze sample in the dark condition, indicating that the greater roughness and lattice distortion are helpful for decreasing the contact angle. This could be because the incorporation of Mg makes the band gap of TiO_2 narrow, thus the visible light can excite pairs of electrons and holes (Figure 11a), just as in the case of ultraviolet irradiation for the pure TiO_2 glaze. Ti^{4+} ions could be united with the photo-induced electron and thus Ti^{3+} ions could be obtained. Ti^{3+} sites can be substituted by Mg^{2+} ions, which produces one excess positive charge. Those excess positive charges could capture the photo-induced electrons quickly, and thus photo-generated holes are available for

combining more H₂O adsorbed on the glaze surface and react with water, producing hydroxyl radicals that are also available for maintaining the hydrophilicity of Mg-doped TiO₂ glaze samples [29]. Therefore, the super-hydrophilicity of Mg-doped TiO₂ glaze samples could be attributed to the visible-light-exciting photo-induced pairs of electrons and holes. For the sample with a V_{water}/V_{ethanol} ratio of 10:5 and 7.5:7.5, the contact angles of water droplets on Mg-doped TiO₂ glaze samples increase slightly, which could be attributed to the decrease in the V_{water}/V_{ethanol} ratio. However, when V_{water}/V_{ethanol} is 10:5 and 7.5:7.5, the hydrophilicity of Mg-doped TiO₂ glaze samples decreases slightly, though it still has super-hydrophilicity. The hydroxy groups anchoring on the Mg-doped TiO₂ glaze surface have a significant impact on the hydrophilicity. The formation of hydroxy groups results in the dissociative adsorption of water molecules at oxygen vacancy sites on the Mg-doped TiO₂ glaze surface. The extra hydroxy groups and oxygen vacancies on the surface are produced by electron–hole pairs, which lead to the hydrophilicity of the Mg-doped TiO₂ glaze surface [39]. Because oxygen vacancy is produced by the doping of Mg in the TiO₂ crystal and the separation of electron–hole pairs is facilitated (Figure 11a), the Mg-doped TiO₂ glaze surface has more photo-induced wettability than the pure TiO₂ glaze surface.

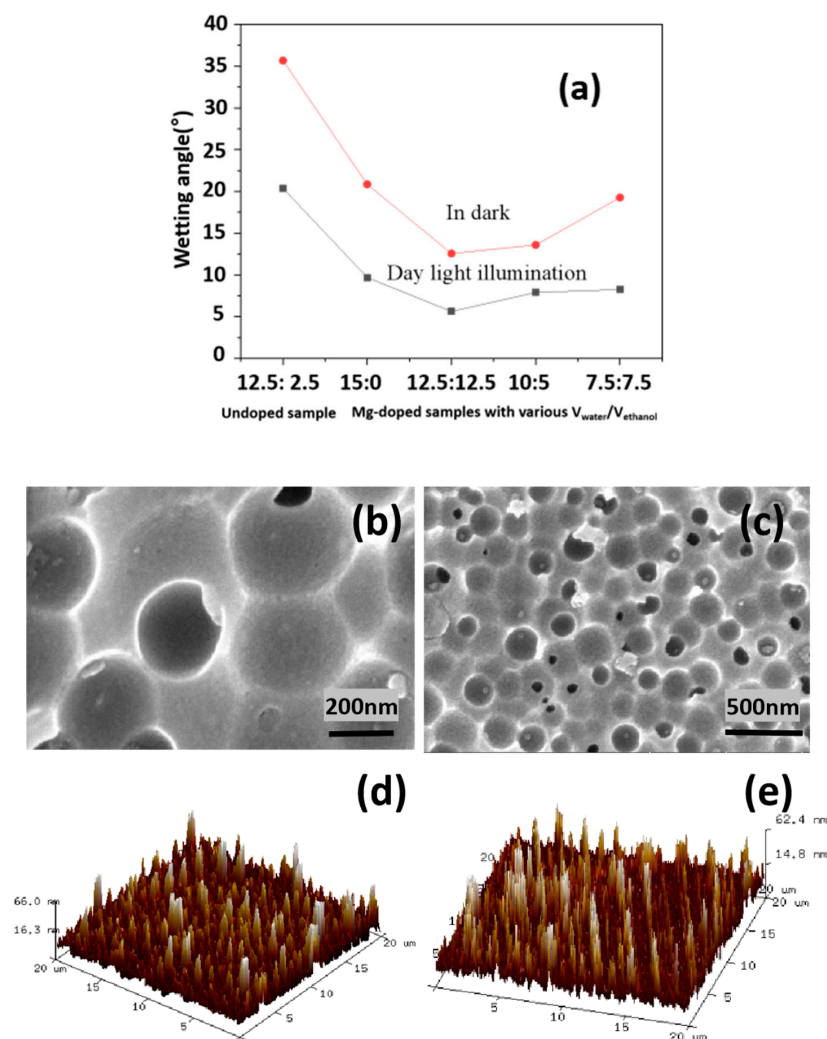


Figure 12. Wetting angle of Mg-undoped TiO₂ glaze sample prepared at V_{water}/V_{ethanol} of 12.5:2.5, and Mg-doped TiO₂ glaze samples with various V_{water}/V_{ethanol} ratios in dark and daylight illumination (a), respectively; SEM images of the Mg-doped TiO₂ glazes prepared using V_{water}/V_{ethanol} of 12.5:2.5 (b) and pure TiO₂ glaze prepared using V_{water}/V_{ethanol} of 12.5:2.5 (c); AFM surfaces of the Mg-doped TiO₂ glaze (d) and pure TiO₂ glaze sample (e) with V_{water}/V_{ethanol} of 12.5:2.5, respectively.

The self-cleaning performance was tested using a Japan Marker pen. The glaze surface was drawn on after drying for 1 h. After that, after placing a few drops of water on the glaze, we could observe whether the ink blots were floating. Table 2 shows that after firing at 1180~1200 °C, the water contact angle (5.623° vs. 15.23°) and stain resistance (the blot floats as a whole vs. not floating, as shown in Figure 13) of the sample fabricated were improved compared to commercial self-cleaning ceramic glazes [49]. The above results indicate the great potential application for enhancing the self-cleaning properties of glazes by introducing Mg-doped TiO₂.

Table 2. Performances of Mg-doped TiO₂ in the ceramic samples obtained in this study and from other literature studies.

| Type | Firing Temperature (°C) | Water Contact Angle (°) | | Stain Resistance | Ref. |
|---|-------------------------|-------------------------|-----------------------|---|-----------|
| | | Before Use | Irradiation after Use | | |
| Mg-doped TiO ₂ in glaze sample | 1180~1200 | 5.623 | 5.124 | After dripping water droplets, the blot floats as a whole | This work |
| TiO ₂ doped in glaze sample | 1180~1200 | 12.26 | 13.56 | Not floating | This work |
| The commercial self-cleaning ceramic products | 1180~1200 | 21.23 | 28.96 | Not floating | This work |
| C-PEG/TiO ₂ coating | - | 26 | 11 | Blot cannot be completely removed | [50] |
| Commercial ceramic tiles with groove-like microstructure surfaces | - | 164.75 | - | Blot cannot be completely removed | [51] |
| Hybrid sol-gel coating and industrial application on polished porcelain stoneware tiles | - | - | - | With the help of cleaning agent, the stains can be removed from the surface | [52] |

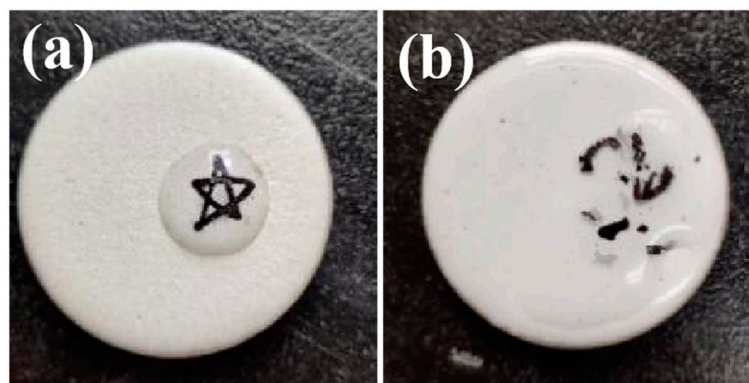


Figure 13. Photos of the as-prepared samples immediately meeting the water in this study (a) Mg-undoped TiO₂ in glaze sample, (b) Mg-doped TiO₂ in glaze sample.

4. Conclusions

In this paper, Mg-doped TiO₂ samples with various $V_{\text{water}}/V_{\text{ethanol}}$ ratios were successfully prepared through the solvothermal method at 180 °C for 36 h. The Mg-doped ($V_{\text{water}}/V_{\text{ethanol}} = 12.5:2.5$) sample had higher surface area, porosity, optical performance, and photocatalytic activity than other samples. Undoped and Mg-doped TiO₂ glaze ceramic samples were prepared using a medium-/high-temperature solid-firing process. Mg-doped TiO₂ samples ($V_{\text{water}}/V_{\text{ethanol}} = 12.5:2.5$) illustrated superior hydrophilicity properties, photocatalytic activity in terms of bleaching organic dye, and self-cleaning capability in ceramic glaze samples than other samples after visible light exposure. This study provides a preparation approach for the synthesis of TiO₂ while controlling crystal size and morphology, which can be utilized with solar energy for bleaching the contaminants in water and enhancing the self-cleaning properties of medium-/high-temperature glazes.

Supplementary Materials: The following supporting information can be downloaded at: <https://www.mdpi.com/article/10.3390/inorganics11080341/s1>, Figure S1: EDX spectroscopy mapping performed in the TEM microscope.

Author Contributions: Conceptualization, T.Z., Q.B. and W.D.; methodology, T.C. and Q.B.; software, P.L. and Y.L.; validation, X.G. and Q.B.; formal analysis, T.Z. and J.Z.; investigation, T.C. and Y.L.; resources, Q.B. and J.Z.; data curation, T.Z. and W.D.; writing—original draft preparation, T.Z. and W.D.; writing—review and editing, T.Z. and W.D.; visualization, P.L. and X.G.; supervision, X.G. and J.Z.; project administration, T.Z. and T.C.; funding acquisition, W.D. All authors have read and agreed to the published version of the manuscript.

Funding: We would like to express our gratitude for the financial support from Major Project of Natural Science Foundation of Jiangxi Province (20232ACB204017), Jingdezhen technology bureau (2021GYZD009-18 and 20224GY008-16) and Jiangxi Province Key R&D Program in China (No. 20202BBE53012), Graduate Innovation Fund Project of Jingdezhen Ceramic University (JYC202004).

Institutional Review Board Statement: Not applicable.

Informed Consent Statement: Not applicable.

Data Availability Statement: The raw data required to reproduce these findings cannot be shared at this time as the data also forms part of an ongoing study.

Conflicts of Interest: The authors declare no conflict of interest.

References

1. Mathew, S.; John, B.K.; Abraham, T.; Mathew, B. Metal-Doped Titanium Dioxide for Environmental Remediation, Hydrogen Evolution and Sensing: A Review. *Chemistryselect* **2021**, *6*, 12742–12751. [[CrossRef](#)]
2. Lettieri, S.; Pavone, M.; Nanostructures, B. Composites and Hybrid Photocatalysts. *Materials* **2022**, *15*, 1271. [[CrossRef](#)] [[PubMed](#)]
3. Jahdi, M.; Mishra, S.B.; Nxumalo, E.N.; Mhlanga, S.D.; Mishra, A.K. Synergistic effects of sodium fluoride (NaF) on the crystallinity and band gap of Fe-doped TiO₂ developed via microwave-assisted hydrothermal treatment. *Opt. Mater.* **2020**, *104*, 109844. [[CrossRef](#)]
4. Wang, Y.; Chen, Y.-X.; Barakat, T.; Wang, T.-M.; Krief, A.; Zeng, Y.-J.; Laboureur, M.; Fusaro, L.; Liao, H.-G.; Su, B.-L. Synergistic effects of carbon doping and coating of TiO₂ with exceptional photocurrent enhancement for high performance H₂ production from water splitting. *J. Energy Chem.* **2021**, *56*, 141–151. [[CrossRef](#)]
5. de Almeida, G.C.; Mohalle, N.D.; Viana, M.M. Ag/GO/TiO₂ nanocomposites: The role of the interfacial charge transfer for application in photocatalysis. *Nanotechnology* **2022**, *33*, 035710. [[CrossRef](#)]
6. Byrne, C.; Dervin, S.; Hermosilla, D.; Merayo, N.; Blanco, A.; Hinder, S.; Harb, M.; Dionysiou, D.D.; Pillai, S.C. Solar light assisted photocatalytic degradation of 1,4-dioxane using high temperature stable anatase W-TiO₂ nanocomposites. *Catal. Today* **2021**, *380*, 199–208. [[CrossRef](#)]
7. Tao, J.; Luttrell, T.; Batzill, M. A two-dimensional phase of TiO₂ with a reduced bandgap. *Nat. Chem.* **2011**, *3*, 296–300. [[CrossRef](#)]
8. Sivkov, A.; Vympina, Y.; Ivashutenko, A.; Rakhmatullin, I.; Shanenkova, Y.; Nikitin, D.; Shanenkov, I. Plasma dynamic synthesis of highly defective fine titanium dioxide with tunable phase composition. *Ceram. Int.* **2022**, *48*, 10862–10873. [[CrossRef](#)]
9. Buchalska, M.; Kobielski, M.; Matuszek, A.; Pacia, M.; Wojtyła, S.; Macyk, W. On oxygen activation at rutile-and anatase-TiO₂. *ACS Catal.* **2015**, *5*, 7424–7431. [[CrossRef](#)]
10. Ji, Y.; Luo, Y. New mechanism for photocatalytic reduction of CO₂ on the anatase TiO₂ (101) surface: The essential role of oxygen vacancy. *J. Am. Chem. Soc.* **2016**, *138*, 15896–15902. [[CrossRef](#)]
11. Estrada-Flores, S.; Martinez-Luevanos, A.; Perez-Berumen, C.M.; Garcia-Cerda, L.A.; Flores-Guia, T.E. Relationship between morphology; porosity, and the photocatalytic activity of TiO₂ obtained by sol-gel method assisted with ionic and nonionic surfactants. *Bol. La Soc. Esp. Ceram. Y Vidr.* **2020**, *59*, 209–218. [[CrossRef](#)]
12. Byrne, C.; Rhatigan, S.; Hermosilla, D.; Merayo, N.; Blanco, A.; Michel, M.C.; Hinder, S.; Nolan, M.; Pillai, S.C. Modification of TiO₂ with hBN: High temperature anatase phase stabilisation and photocatalytic degradation of 1,4-dioxane. *J. Phys.-Mater.* **2020**, *3*, 015009. [[CrossRef](#)]
13. Yu, Z.H.; Zhu, S.L.; Zhang, L.H.; Watanabe, S. Mesoporous single crystal titanium oxide microparticles for enhanced visible light photodegradation. *Opt. Mater.* **2022**, *127*, 112297. [[CrossRef](#)]
14. Kumar, A.; Choudhary, P.; Krishnan, V. Selective and efficient aerobic oxidation of benzyl alcohols using plasmonic Au-TiO₂: Influence of phase transformation on photocatalytic activity. *Appl. Surf. Sci.* **2022**, *578*, 151953. [[CrossRef](#)]
15. Wu, J.M.; Xing, H. Facet-dependent decoration of TiO₂ mesocrystals on TiO₂ microcrystals for enhanced photoactivity. *Nanotechnology* **2020**, *31*, 025604. [[CrossRef](#)] [[PubMed](#)]
16. Song, C.G.; Won, J.; Jang, I.; Choi, H. Fabrication of high-efficiency anatase TiO₂ photocatalysts using electrospinning with ultra-violet treatment. *J. Am. Ceram. Soc.* **2021**, *104*, 4398–4407. [[CrossRef](#)]

17. George, S.; Pokhrel, S.; Ji, Z.; Henderson, B.L.; Xia, T.; Li, L.; Zink, J.I.; Nel, A.E.; Mädler, L. Role of Fe doping in tuning the band gap of TiO₂ for the photo-oxidation-induced cytotoxicity paradigm. *J. Am. Chem. Soc.* **2011**, *133*, 11270–11278. [[CrossRef](#)] [[PubMed](#)]
18. Galindo-Hernandez, F.; Gomez, R.; De la Torre, A.I.R.; Mantilla, A.; Lartundo-Rojas, L.; Martinez, A.M.M.; Cipagauta-Diaz, S. Structural changes and photocatalytic aspects into anatase network after doping with cerium: Comprehensive study via radial distribution functions, electron density maps and molecular hardness. *J. Photochem. Photobiol. A-Chem.* **2022**, *428*, 113855. [[CrossRef](#)]
19. Shymanovska, V.V.; Khalyavka, T.A.; Manuilov, E.V.; Gavrilko, T.A.; Aho, A.; Naumov, V.V.; Shcherban, N.D. Effect of surface doping of TiO₂ powders with Fe ions on the structural, optical and photocatalytic properties of anatase and rutile. *J. Phys. Chem. Solids* **2022**, *160*, 110308. [[CrossRef](#)]
20. Huang, J.X.; Li, D.G.; Li, R.B.; Chen, P.; Zhang, Q.X.; Liu, H.J.; Lv, W.Y.; Liu, G.G.; Feng, Y.P. One-step synthesis of phosphorus/oxygen co-doped g-C₃N₄/anatase TiO₂ Z-scheme photocatalyst for significantly enhanced visible-light photocatalysis degradation of enrofloxacin. *J. Hazard. Mater.* **2020**, *386*, 121634. [[CrossRef](#)]
21. Sudrajat, H.; Babel, S.; Hartuti, S.; Phanthuwongpakdee, J.; Laohasurayotin, K.; Nguyen, T.K.; Tong, H.D. Origin of the overall water splitting activity over Rh/Cr₂O₃@anatase TiO₂ following UV-pretreatment. *Int. J. Hydrog. Energy* **2021**, *46*, 31228–31238. [[CrossRef](#)]
22. Alshehri, A.; Narasimharao, K. PtOx-TiO₂ anatase nanomaterials for photocatalytic reformation of methanol to hydrogen: Effect of TiO₂ morphology. *J. Mater. Res. Technol.-JmrT* **2020**, *9*, 14907–14921. [[CrossRef](#)]
23. Zhang, Q.; Li, C.Y. Effects of water-to-methanol ratio on the structural, optical and photocatalytic properties of titanium dioxide thin films prepared by mist chemical vapor deposition. *Catal. Today* **2020**, *358*, 172–176. [[CrossRef](#)]
24. Alotaibi, A.M.; Williamson, B.A.D.; Sathasivam, S.; Kafizas, A.; Alqahtani, M.; Sotelo-Vazquez, C.; Buckeridge, J.; Wu, J.; Nair, S.P.; Scanlon, D.O.; et al. Enhanced Photocatalytic and Antibacterial Ability of Cu-Doped Anatase TiO₂ Thin Films: Theory and Experiment. *ACS Appl. Mater. Inter.* **2020**, *12*, 15348–15361. [[CrossRef](#)] [[PubMed](#)]
25. Wang, Q.Y.; Li, H.L.; Yu, X.L.; Jia, Y.; Chang, Y.; Gao, S.M. Morphology regulated Bi₂WO₆ nanoparticles on TiO₂ nanotubes by solvothermal Sb³⁺ doping as effective photocatalysts for wastewater treatment. *Electrochim. Acta* **2020**, *330*, 135167. [[CrossRef](#)]
26. Li, J.; Chu, B.X.; Xie, Z.; Deng, Y.Q.; Zhou, Y.M.; Dong, L.H.; Li, B.; Chen, Z.J. Mechanism and DFT study of degradation of organic pollutants on rare earth ions doped TiO₂ photocatalysts prepared by sol-hydrothermal synthesis. *Catal. Lett.* **2022**, *152*, 489–502. [[CrossRef](#)]
27. Nithya, N.; Gopi, S.; Bhoopathi, G. An Amalgam of Mg-Doped TiO₂ Nanoparticles Prepared by Sol-Gel Method for Effective Antimicrobial and Photocatalytic Activity. *J. Inorg. Organomet. Polym. Mater.* **2021**, *31*, 4594–4607. [[CrossRef](#)]
28. Barbierikova, Z.; Dvoranova, D.; Sofianou, M.V.; Trapalis, C.; Brezova, V. UV-induced reactions of Mg²⁺-doped anatase nanocrystals with exposed {001} facets: An EPR study. *J. Catal.* **2015**, *331*, 39–48. [[CrossRef](#)]
29. Cao, T.H.; Liang, Y.Z.; Bao, Q.F.; Xu, C.L.; Bai, M.M.; Luo, T.; Gu, X.Y. A simple solvothermal preparation of Mg-doped anatase TiO₂ and its self-cleaning application, solar energy. *Sol. Energy* **2023**, *249*, 12–20. [[CrossRef](#)]
30. Sheldrick, G.M. Phase annealing in SHELX-90: Direct methods for larger structures. *Acta Crystallogr. Sect. A Found. Crystallogr.* **1990**, *46*, 467–473. [[CrossRef](#)]
31. Cullity, B.D. *Elements of X-ray Diffraction*, 2nd ed.; Addison-Wesley: London, UK, 1978.
32. Olowoyo, J.O.; Kumar, M.; Singhal, N.; Jain, S.L.; Babalola, J.O.; Vorontsov, A.V.; Kumar, U. Engineering and modeling the effect of Mg doping in TiO₂ for enhanced photocatalytic reduction of CO₂ to fuels. *Catal. Sci. Technol.* **2018**, *8*, 3686–3694. [[CrossRef](#)]
33. Dong, W.X.; Zhao, G.L.; Song, B.; Xu, G.; Zhou, J.; Han, G.R. Surfactant-free fabrication of CaTiO₃ butterfly-like dendrite via a simple one-step hydrothermal route. *Crystengcomm* **2012**, *14*, 6990–6997. [[CrossRef](#)]
34. Zhang, J.; Sun, P.; Jiang, P.; Guo, Z.; Liu, W.; Lu, Q.; Cao, W. The formation mechanism of TiO₂ polymorphs under hydrothermal conditions based on the structural evolution of [Ti(OH)_h(H₂O)_{6-h}]^{4-h} monomers. *J. Mater. Chem. C* **2019**, *7*, 5764–5771. [[CrossRef](#)]
35. Kolker, A.; Pablo, J. Thermodynamic modeling of concentrated aqueous. *Ind. Eng. Chem. Res.* **1996**, *35*, 228–233. [[CrossRef](#)]
36. Wang, C.C.; Wang, K.W.; Perng, T.P. Electron field emission from Fe-doped TiO₂ nanotubes. *Appl. Phys. Lett.* **2010**, *96*, 143102. [[CrossRef](#)]
37. Wang, Q.; Li, H.J.; Zhang, R.X.; Liu, Z.Z.; Deng, H.Y.; Cen, W.G.; Yan, Y.G.; Chen, Y.G. Oxygen vacancies boosted fast Mg²⁺ migration in solids at room temperature. *Energy Storage Mater.* **2022**, *51*, 630–637. [[CrossRef](#)]
38. Ali, T.; Ahmed, A.; Siddique, M.N.; Alam, U.; Muneer, M.; Tripathi, P. Influence of Mg²⁺ ion on the optical and magnetic properties of TiO₂ nanostructures: A key role of oxygen vacancy. *Optik* **2020**, *223*, 165340. [[CrossRef](#)]
39. Dong, W.X.; Song, B.; Zhao, G.L.; Han, G.R. Controllable synthesis of CaTi₂O₄(OH)₂ nanoflakes by a facile template-free process and its properties. *Ceram. Int.* **2013**, *39*, 6795–6803. [[CrossRef](#)]
40. Nakamoto, K. *Infrared and Raman Spectra of Inorganic and Coordination Compounds, Part B: Applications in Coordination, Organometallic, and Bioinorganic Chemistry*; John Wiley & Sons: New York, NY, USA, 2009.
41. Shivaraju, H.P.; Yashas, S.R.; Harini, R. Application of Mg-doped TiO₂ coated buoyant clay hollow-spheres for photodegradation of organic pollutants in wastewater. *Mater. Today Proc.* **2020**, *27*, 1369–1374. [[CrossRef](#)]
42. Deng, R.H.; Liu, S.H.; Li, J.Y.; Liao, Y.G.; Tao, J.; Zhu, J.T. Mesoporous block copolymer nanoparticles with tailored structures by hydrogen-bonding-assisted self-assembly. *Adv. Mater.* **2012**, *24*, 1889–1893. [[CrossRef](#)]

43. Huang, W.; Cheng, H.; Feng, J.; Shi, Z.; Bai, D.; Li, L. Synthesis of highly water-dispersible N-doped anatase titania based on low temperature solvent-thermal method. *Arab. J. Chem.* **2018**, *11*, 871–879. [[CrossRef](#)]
44. Singh, M.K.; Mehata, M.S. Enhanced photoinduced catalytic activity of transition metal ions incorporated TiO₂ nanoparticles for degradation of organic dye: Absorption and photoluminescence spectroscopy. *Opt. Mater.* **2020**, *109*, 110309. [[CrossRef](#)]
45. Bally, A.R.; Korobeinikova, E.N.; Schmid, P.E.; Levy, F.; Bussy, F. Structural and electrical properties of Fe-doped thin films. *J. Phys. D Appl. Phys.* **1998**, *31*, 1149. [[CrossRef](#)]
46. Hoffmann, M.R.; Martin, S.T.; Choi, W.; Bahnemann, D.W. Environmental applications of semiconductor photocatalysis. *Chem. Rev.* **1995**, *95*, 69–96. [[CrossRef](#)]
47. Augugliaro, V.; Loddo, V.; Marci, G.; Palmisano, L.; López-Muñoz, M.J. Photocatalytic oxidation of cyanides in aqueous titanium dioxide suspensions. *J. Catal.* **1997**, *166*, 272–283. [[CrossRef](#)]
48. Zubair, M.A.; Al Mamun, A.; McNamara, K.; Tofail, S.A.M.; Islam, F.; Lebedev, V.A. Amorphous interface oxide formed due to high amount of Sm doping (5–20 mol%) stabilizes finer size anatase and lowers indirect band gap. *Appl. Surf. Sci.* **2020**, *529*, 146967. [[CrossRef](#)]
49. Ferreira-Neto, E.P.; Ullah, S.; Martinez, V.P.; Yabarrena, J.M.C.; Simões, M.B.; Perissinotto, A.P.; Wender, H.; De Vicente, F.S.; Noeske, P.-L.M.; Ribeiro, S.J. Thermally stable SiO₂@TiO₂ core@shell nanoparticles for application in photocatalytic self-cleaning ceramic tiles. *Mater. Adv.* **2021**, *2*, 2085–2096. [[CrossRef](#)]
50. Kim, S.M.; In, I.; Park, S.Y. Study of photo-induced hydrophilicity and self-cleaning property of glass surfaces immobilized with TiO₂ nanoparticles using catechol chemistry. *Surf. Coat. Technol.* **2016**, *294*, 75–82. [[CrossRef](#)]
51. Li, K.; Yao, W.; Liu, Y.; Wang, Q.; Jiang, G.; Wu, Y.; Lu, L. Wetting and anti-fouling properties of groove-like microstructured surfaces for architectural ceramics. *Ceram. Int.* **2022**, *48*, 6497–6505. [[CrossRef](#)]
52. Akarsu, M.; Burunkaya, E.; Tunali, A.; Selli, N.T.; Arpaç, E. Enhancement of hybrid sol-gel coating and industrial application on polished porcelain stoneware tiles and investigation of the performance. *Ceram. Int.* **2014**, *40*, 6533–6540. [[CrossRef](#)]

Disclaimer/Publisher's Note: The statements, opinions and data contained in all publications are solely those of the individual author(s) and contributor(s) and not of MDPI and/or the editor(s). MDPI and/or the editor(s) disclaim responsibility for any injury to people or property resulting from any ideas, methods, instructions or products referred to in the content.